Constraints on North Anatolian Fault zone width in the crust and upper mantle from S-wave teleseismic tomography

E. Papaleo[1], D. G. Cornwell[1], and N. Rawlinson[2]

[1]School of Geosciences, University of Aberdeen, King's College, Aberdeen, AB24 3UE, UK
[2]Department of Earth Sciences, Bullard Laboratories, University of Cambridge, Madingley Road, Cambridge, CB3 0EZ, UK

Key Points:

- An ~15-km resolution teleseismic S-wave velocity model constrains width and depth of the North Anatolian Fault in the crust and upper mantle
- The northern branch of the NAFZ is ≤10 km wide in the upper crust, widens to ~30 km in the lower crust and continues into the upper mantle
- The southern branch of the North Anatolian Fault is likely a narrow weak zone within a complex juxtaposition of stronger lithospheric blocks

Corresponding author: Elvira Papaleo, `elvira.papaleo@abdn.ac.uk`

Abstract

We present high resolution S-wave teleseismic tomography images of the western segment of the North Anatolian Fault (NAFZ) in Turkey using teleseismic data recorded during the deployment period of the DANA array. The array comprised 66 stations with a nominal station spacing of 7 km, thus permitting a horizontal and vertical resolution of approximately 15 km. We use the current S-wave results with previously published P-wave teleseismic tomography to produce maps of relative V_P/V_S anomalies, which we use to highlight the difference in overall composition of the three terranes separated by the northern (NNAF) and southern (SNAF) branches of the NAFZ. Our results show a narrow S-wave low velocity anomaly beneath the northern branch of the NAFZ extending from the upper crust, where it has a width of ~10 km, to the lower crust, where it widens to ~30 km. This low velocity zone most likely extends into the upper mantle, where we constrain its width to be ≤50 km and interpret it as indicative of localised shear beneath the NNAF; this structure is similar to what has been observed for the NAFZ west of 32° and therefore we propose that the structure of the NNAF is similar to that of the NAFZ in the east. The SNAF does not show a very strong signature in our images and we conclude that it is most likely rooted in the crust, possibly accommodating deformation related to rotation of the Armutlu/Almacik Blocks situated between the two NAFZ branches.

1 Introduction

Continental strike-slip faults, such as the North Anatolian, San Andreas, Altyn Tagh and Alpine faults, are major structures accommodating the relative movement between tectonic plates. Whether or not intracontinental strike-slip faults are rooted in the middle to lower crust or penetrate the upper mantle, however, is still a subject of debate (e.g. *Sibson* [1983]; *Vauchez and Tommasi* [2003]; *Wilson et al.* [2004]). In this study we exploit passive seismic data to image the western section of the North Anatolian Fault Zone (NAFZ) in Turkey, a dextral continental strike-slip fault which extends for approximately 1200 km across the north of the Anatolian peninsula (Fig. 1). Our aim is to understand its structure in the mid-lower crust and examine the extent to which it penetrates into the upper mantle.

The inception of the North Anatolian Fault occurred between 13 and 11 Ma (*Şengör et al.* [2005]), and came about due to the confluence of two factors: the push of the Arabian plate towards the Eurasian plate in the southeast and subduction along the Aegean arc in the west. However, the importance of these two tectonic events and the mechanisms that drive them in present day motion of the Anatolian peninsula are debated (e.g. *Reilinger et al.* [2006]; *Özeren and Holt* [2010]; *England et al.* [2016]). Geological evidence (*Şengör et al.* [2005]) supports the notion that the NAFZ, after inception in eastern Turkey, progressed westward and only reached the Marmara Sea approximately 4 Ma ago (*Le Pichon et al.* [2016]). The NAFZ is seismically active and has experienced a series of migrating earthquakes in the last century (*Stein et al.* [1997]), the most recent of which were the M>7 Izmit and Düzce events in northern Anatolia in 1999 (Fig. 1).

Geophysical signatures of the NAFZ to the east of our study area (Fig. 1), before it splays into northern and southern branches, can be found in several studies; *Biryol et al.* [2011] found that the NAFZ forms a rather sharp, lithospheric scale structural boundary, separating older lithosphere of the north Anatolian province and the younger central Anatolian province. A substantial north-south increase in Bouguer anomaly across the NAFZ also supports these findings and may indicate an increase in crustal density to the north (*Ates et al.* [1999]). Results from full waveform inversion (*Fichtner et al.* [2013]) image, along strike, low S-wave velocities linking the crustal expression of the NAFZ to a broad (i.e. 50-100 km wide at 60 km depth) region of low velocity in the mantle, however, the authors note that no clear signature of the NAFZ can be seen west of 32°, where our current study is located. In addition, low upper-crustal velocities ($V_P \leq 6$ km/s at depths of 5-15 km) along the NAFZ in central Anatolia were also reported by a local earthquake tomography study (*Yolsal-Çevikbilen et al.* [2012]).

Recent studies on the western portion of the NAFZ (Fig. 1) revealed additional information on the structure of its two strands. The presence of different lithologies bounding the northern branch of the NAFZ has been inferred by *Bulut et al.* [2012] and *Najdahmadi et al.* [2016] by tracking fault head waves caused by the presence of a bimaterial interface. This is also consistent with a change in Moho signature and depth observed in the Istanbul Zone and has been attributed to either the presence of a thicker crust (*Frederiksen et al.* [2015]) or a weak Moho underlain by a highly anisotropic layer (*Kahraman et al.* [2015]). These observations support the idea that a clear separation between the north Anatolian province and the central Anatolian province exists across the northern NAFZ. Receiver function and autocorrelation studies (*Kahraman et al.* [2015]; *Taylor et al.* [2016]) reported truncation of several sub-horizontal structures throughout the crust beneath both NAFZ strands. Furthermore, an absence of Moho signature beneath the northern NAFZ may indicate a fault zone rooted in the upper mantle (*Kahraman et al.* [2015]). Results from P wave teleseismic tomography in the same area (*Papaleo et al.* [2017]) provided the first direct evidence for a narrow (<50 km) fault zone that extends into the upper mantle to a depth of at least 80 km beneath the northern branch of the NAFZ.

The S wave teleseismic tomography presented in this study, together with a $\delta(V_P/V_S)$ model obtained by combining our S and P wave results (*Papaleo et al.* [2017]), complements the P wave study and effectively outlines different characteristics of the two fault strands. We are able to map the northern branch of the NAFZ (NNAF) as a low velocity anomaly from crust to upper mantle using our new S-wave velocity model, while highlighting major differences in crustal geology with the $\delta(V_P/V_S)$ model. We discuss our findings in terms of fault structure and the evolution of fault width with depth.

2 Data and methods

In this study we use teleseismic data collected during the operational period of the DANA (Dense Array for Northern Anatolia, 2012) array (*Brisbourne* [2012]), composed of 73 broadband stations deployed between May 2012 and October 2013. The main array comprises 66 stations covering an area of approximately 70 x 35 km with a 7 km nominal station spacing; the remaining stations were deployed in a semicircle around the main array to the east (Fig. 1). A total of 10,650 arrival time residuals from 198 events have been used to perform the S wave teleseismic tomography; of these events, 98 are direct S wave arrivals, 55 are SKS arrivals, 25 are SKKS arrivals and 20 are SS arrivals (Fig. 2).

The north-south and east-west components recorded by the instruments were rotated into transverse and radial components and filtered between 0.04 and 0.5 Hz with a Butterworth bandpass filter. To check the dependence of the results on the use of a particular component, we carried out two separate inversions using recordings from solely radial and solely transverse components. We found that the final results do not differ significantly, therefore, we selected the component with the highest signal to noise ratio for each event in the final inversion.

Relative arrival time residuals were obtained using an adaptive stacking technique (*Rawlinson and Kennett* [2004]), which is particularly effective in this setting because teleseismic waveforms are coherent across the array. This method works by initially aligning phases from a single event using move-out correction based on ak135 global reference model. The remaining time shifts required to perfectly align the phases correspond to the arrival time residuals which can be attributed to lateral variations in wavespeed beneath the array. Since there is no absolute reference frame for the alignment, the arrival time residuals are meaningful in a relative rather than absolute sense. The results of the stacking procedure were manually checked to eliminate all traces with poor signal to noise ratio. In addition, all residuals with a discrepancy between observed and predicted values greater than 0.5 s after an initial inversion, were removed to improve the final model. To perform the tomography, we use the Fast Marching Teleseismic Tomography code (*Rawlinson et al.* [2006]), an iterative method based on subspace inversion (*Kennett et al.* [1988]) and the Fast Marching Method (*Sethian* [1999]) to compute arrival times through the laterally heterogeneous model volume. Traveltimes from the source to the boundary of the local model volume are based on ak135 predictions. The final velocity model is computed by minimising the function

$$F(\mathbf{m}) = \frac{1}{2}[\Phi(\mathbf{m}) + \epsilon\Psi(\mathbf{m}) + \eta\Omega(\mathbf{m})], \tag{1}$$

where $\mathbf{m}$ is the vector of model parameters, $\Phi(\mathbf{m})$ is the data misfit function, $\Psi(\mathbf{m})$ the model misfit function (i.e. misfit of the current model with respect to the starting model) and $\Omega(\mathbf{m})$ constrains the model roughness; ϵ and η are the damping and smoothing parameters which control the overall trade-off between how well the model $\mathbf{m}$ fits the data, how close it is to the starting model and how smooth it is.

The local 3D volume used in this inversion, extending to a depth of 100 km, is defined by a grid with a 5 km node spacing in all directions. Reference 1D velocities within the volume (Table 1) are modified from the general ak135 velocity model, taking into consideration seismic refraction and receiver function derived velocity models from previous studies in the same area (*Karahan et al.* [2001]; *Kahraman et al.* [2015]). We also set our Moho depth at 37 km in accordance with previous receiver function studies (*Vanacore* [2013]; *Kahraman et al.* [2015]) and to be consistent with our previous P wave teleseismic tomography study in the same area (*Papaleo et al.* [2017]). However, we note that the Moho in the inversion is not explicitly expressed as an additional interface in the model; instead it is represented by a sharp velocity gradient. Station terms are inverted for and, prior to the final inversion, damping and smoothing parameters were calibrated to obtain a good trade-off between data fit, model perturbation and roughness (see Supplementary Figures S3, S4, S5 and S6 for further details).

Table 1. Background velocity model used for the inversion (velocity model taken from *Kahraman et al.* [2015]).

Depth(km)	Vp(km/s)	Vs(km/s)	V_P/V_S
0	3.776	2.128	1.774
2	3.776	2.128	1.774
2	5.194	2.928	1.774
13	5.194	2.928	1.774
13	6.286	3.540	1.776
24	6.484	3.717	1.744
37	6.484	3.717	1.744
37	7.539	4.367	1.726
77	8.045	4.490	1.792

A number of synthetic tests have been carried out on the data to assess the resolution of our tomographic model. Checkerboard test results (Fig. 3) indicate that there is good recovery of the original velocity anomaly pattern to 80 km depth (the maximum input velocity perturbation being 0.35 km/s), with a more pronounced (up to 50%) loss in amplitude below 50 km depth. The original pattern of anomalies is especially well resolved in the area beneath the stations, where we observe a very good recovery of 15 km size anomalies both horizontally and vertically. Spike test results (see Supplementary Figures S7 and S8) show that horizontal smearing (relative to our choice of input anomaly) is modest in the upper mantle (±2 km) and largely absent at crustal and Moho depth, while vertical smearing is more pronounced and generally within ±8 km. We quantify amplitude loss to be less than 30% in the crust but more significant in the upper mantle, where we observe an approximately 50% reduction in amplitude at 70 km depth.

2.1 $\delta(V_P/V_S)$ estimate

To obtain additional information on the seismic properties of our study area, we produced $\delta(V_P/V_S)$ estimates using the results obtained from P and S wave tomography. Table 1 provides the initial V_P/V_S values, which are, on average, similar to results from local earthquake tomography studies (*Koulakov et al.* [2010]; *Yolsal-Çevikbilen et al.* [2012]).

Although there are teleseismic studies that constrain variations in V_P/V_S by jointly inverting P and S datasets (e.g. *Hammond and Toomey* [2003], *Schmandt and Humphreys* [2010]), we note that V_P/V_S estimates are not usually obtained from teleseismic data, which constrain relative rather than absolute velocities. In particular in this study, rather than the absolute V_P/V_S ratio, we are looking for perturbation in the V_P/V_S ratio (see Supplemetary Text S1 for a full derivation):

$$\delta\left(\frac{V_P}{V_S}\right) = \frac{\delta V_P - C\delta V_S}{V_S^0 + \delta V_S}, \tag{2}$$

where $C = V_P^0/V_S^0$, V_P^0 and V_S^0 are reference model velocities and δV_P and δV_S their respective perturbations. In this case the sign of the perturbation depends the sign of the numerator $(\delta V_P - C\delta V_S)$; therefore, if the model V_P/V_S ratio is too high, it will result in overly negative perturbations and if it is too low in overly positive perturbations; however, the relative perturbations are likely robust. Nevertheless, different initial values of V_P/V_S ratio were tested to ensure that the changes do not affect our results significantly (see Supplementary Figures S11 and S12). In addition to ensure that the $\delta(V_P/V_S)$ anomalies that we obtain are robust, we performed several tests to ensure that the recovered anomalies are not the result of arbitrary initial parameter choices, variable data coverage or solution non-uniqueness (see Supplementary Figures S9 and S10). As an additional measure, we only interpret the final results in terms of broad changes in $\delta(V_P/V_S)$ pattern rather than absolute perturbations.

First, $\delta(V_P/V_S)$ plots were obtained only using direct P and S arrivals and, to ensure an even coverage, we only used traces for which both P and S recordings were available. The initial results were tested by varying the damping and smoothing parameters in eq. 1 for P and S inversions independently, using values of 1, 2, 5 and 10. After checking that the results obtained by using all these different combinations of values were broadly consistent with each other, we chose final damping and smoothing values of 10 and 5 for P and 5 and 2 for S respectively. The final parameters were found to yield good results both in the independent inversion of P and S waves and the final $\delta(V_P/V_S)$ results. In addition, we also checked our results by fixing the damping and smoothing parameters and varying the initial velocity model. Checkerboard tests for V_P, V_S and $\delta(V_P/V_S)$ using the aforementioned subset of data demonstrate that data recovery is most robust in the uppermost 40 km; therefore we limit our interpretation to crustal features (see Supplementary Figures S14 and S15).

3 Results

3.1 Relative S wave model

We present our results in Figures 4 and 5; all velocities are expressed in percentage variation with respect to the starting model in Table 1. Overall, relatively low velocities (-2 to -3%) are constrained in the Sakarya Zone to Moho depths and a relatively high velocity anomaly (+1%) is imaged between the two branches of the NAFZ in the Armutlu Block. The Istanbul Zone, in the north of our study area, predominantly exhibits relatively high velocities (+1 to +2%), with the exception of a ~20 km band of relatively low velocities (-1%) oriented broadly east-west. Depth slices shown in Figure 4 demonstrate that the velocity patterns are generally consistent between the upper and lower crust. However, below the Moho, we observe a change in the pattern of velocity anomalies from an east-west alignment that is consistent with first order changes in the surface geology at the major NAFZ branches and the highest density of seismicity, to a north-south to northeast-southwest alignment of velocity anomalies in the upper mantle (Fig. 4)

Our north-south profiles (Fig. 5) span an area between 30.1 and 30.5° E, where we have the best resolution in our model. We consistently observe relatively high velocities (up to 2%) in the crust north of the northern branch of the NAFZ (NNAF), while in close proximity to the surface trace of the NAFZ velocities are relatively low (approximately -1%). In all our vertical profiles, the low velocity anomaly beneath the NNAF extends from the upper crust, where its width is constrained to be ~10 km, to the lower crust, where it widens to ~30 km, and penetrates into the upper mantle. In the western profiles (Fig. 5b), this low velocity anomaly merges with a broader upper mantle low velocity anomaly extending for approximately 80 km in a north-south direction.

A relatively high velocity anomaly (up to 2%) is situated in the Armutlu Block between the two branches of the NAFZ and is visible in all profiles; this anomaly is narrower (~10 km) and confined to the crust in the west, while it increases in volume eastward where, approximately at Moho depths, it widens (up to 30 km) towards the Sakarya Zone and extends into the upper mantle.

The southern branch of the NAFZ (SNAF) and the area to its south exhibit the lowest velocity anomaly imaged in our model (peak perturbation of -3%). The low velocity anomaly beneath the SNAF extends perpendicular to the NAFZ for approximately 40 km in the crust and, with the exception of the profile at 30.1° E, only extends into the upper mantle south of 40.3 ° N. It is cut for most of its horizontal length by the relatively high (+1 to + 2%) velocity body between the two strands of the NAFZ.

3.2 $\delta(V_P/V_S)$ model

As described in Section 2.1, the $\delta(V_P/V_S)$ model adds an interpretative tool which complements the S wave tomography model presented in this study and the P wave tomography model presented in *Papaleo et al.* [2017]. Figure 6c shows $\delta(V_P/V_S)$ results in two vertical profiles, together with the respective P and S wave velocity profiles. Results are also, in this case, shown as a percentage variation with respect to an initial velocity model (Table 1). Overall, we observe lower $\delta(V_P/V_S)$ anomalies in the Istanbul Zone and generally higher (up to 3%) $\delta(V_P/V_S)$ values in both the Sakarya Zone and Armutlu Block; the highest values are observed south of the SNAF in the upper crust of the Sakarya Zone. We also note that the overall pattern of $\delta(V_P/V_S)$ anomalies changes between upper and lower crust, particularly beneath the SNAF, NNAF and Istanbul Zone, where there is a polarity reversal in $\delta(V_P/V_S)$ anomaly.

We now examine the characteristics of our $\delta(V_P/V_S)$ model where prominent anomalies are identified in the V_S tomography model (i.e. beneath the surface location of the NNAF and first order variations between the Istanbul Zone, Armutlu Block and Sakarya Zone) using the two best resolved north-south profiles (Fig. 6e, f).

The NNAF is clearly situated at an abrupt lateral variation between $\delta(V_P/V_S)$ values of -2% to the north and +2% to the south (Fig.6e, f). This characteristic of the $\delta(V_P/V_S)$ model extends west-east over 60 km and correlates closely with the surface trace of the NNAF and elevated rates of seismicity (*Altuncu-Poyraz et al.* [2015]). This sharp lateral change in $\delta(V_P/V_S)$ appears as a sub-vertical pronounced velocity gradient to depths of 15-20 km in our model (corresponding to the seismogenic depth), but either does not extend deeper or is offset northwards by ~10 km in the lower crust. $\delta(V_P/V_S)$ values north of the NNAF, in the Istanbul Zone, are characteristically the lowest observed in our model (−2 to − 3%) but may increase northwards.

In general, Armutlu Block crust is characterised by medium to high $\delta(V_P/V_S)$ values between 0.5-2.5%, whereas Sakarya Zone crust displays the highest $\delta(V_P/V_S)$ values in our model (> 2.5%). This first-order change occurs at the surface location of the SNAF, which is marked by a slight reduction in $\delta(V_P/V_S)$ within a <10 km wide zone (noting that we can recover anomalies ~7 in size in the upper region of our model - see Supplementary Figure 5) that may extend from the surface into the mid-lower crust. This feature, although not prominent in all of our profiles, is the first indication from any velocity model of the presence and structure of the SNAF within the crust and correlates well with SNAF-related seismicity (*Altuncu-Poyraz et al.* [2015], Fig. 6f).

4 Interpretation

4.1 NNAF

Our S wave velocity model constrains a ~15 km wide low velocity zone (-1 to -2%) in the upper crust directly beneath the surface trace of the NNAF; low velocities are often associated with fault zones (e.g. *Smith et al.* [1995]; *Wittlinger et al.* [1998]; *Fichtner et al.* [2013]) and are thought to occur due to fracturing and the presence of fluids (e.g. *Koulakov et al.* [2010]) or the presence of a fault damage zone (e.g. *Hong and Menke* [2006]; *Allam and Ben-Zion* [2012]). Through plotting the seismicity that occurred during the DANA deployment period (*Altuncu-Poyraz et al.* [2015]) onto our velocity images (Figs. 4, 5, 6), it is clear that the currently most actively deforming parts of the upper crust coincide with our major low velocity zone and strongest $\delta(V_P/V_S)$ lateral change beneath the NNAF (Figs. 5b, 6c and 6e), therefore we interpret our results to be consistent with the presence of a localised damage zone in the upper crust beneath the NNAF at a major geological interface. We note, however, that not all seismicity coincides with our anomalies and we observe that clusters of off-fault events occur in the high velocity region north of the NNAF (Fig. 5d).

A similar V_P/V_S pattern to that observed beneath the NNAF (relatively higher $\delta(V_P/V_S)$ south of the fault and relatively lower $\delta(V_P/V_S)$ to the north) has also been imaged at other major fault zones (e.g. *Lin and Thurber* [2012]; *Eberart-Philips et al.* [2005]) and we interpret it to result from lithological differences between the older Istanbul Zone and the younger Armutlu Peninsula terranes, also observed by previous teleseismic studies (*Biryol et al.* [2011]). Clear signatures of the presence of the NNAF in the upper crust in this region can also be found in other studies, for example, *Bulut et al.* [2012] find a 6 % change in the velocity of fault head waves across the northern branch of the fault, which is similar to the 3-4 % change in velocity according to our P and S wave velocity models (particularly bearing in mind that the magnitude of the perturbations might be underestimated in the tomography) and a reduction (of 0.2 to 0.6 km/s) in absolute P wave velocity beneath the fault (*Behyan and Alkan* [2015]).

Discontinuities throughout the crust mapped by a previous receiver function study (*Kahraman et al.* [2015]) are plotted in Figs. 6c and 6d and their truncation occurs where we constrain lateral changes in crustal velocity structure and where either Moho discontinuity amplitude is reduced (*Kahraman et al.* [2015]) or there is a step in Moho depth (*Frederiksen et al.* [2015]). In a similar location beneath the NNAF, magnetotelluric studies (e.g. *Tank et al.* [2005]) show a boundary in the mid to lower crust between a resistive body to the north and a conductive body to the south. We expect that below seismogenic depths (15-20 km in our study area) fault deformation is likely going to be localised within mylonite belts (e.g. *Sibson* [1983]; *Norris and Toy* [2014]), the extent of which, from a combination of results from this and the aforementioned studies, is likely to be ~10 km in the upper crust, widening to ~30 km in the lower crust.

The relatively low velocity zone that we observe beneath the NNAF most likely extends into the upper mantle (Figs. 4 and 5), where it widens to ≤50 km. We note that while our synthetic resolution tests indicate that the resolution decreases below ~40 km depth (see Fig. 3), it is still sufficient to support the increase in width of the low velocity zone with depth. Therefore, following interpretation of low upper mantle velocity anomalies in previous studies using similar techniques (e.g. *Wittlinger et al.* [1998]; *Vauchez and Tommasi* [2003]), we interpret this anomaly as localised shear beneath the NNAF.

4.2 SNAF

We note that our $\delta(V_P/V_S)$ maps (Fig. 6c) show up to a 2% lateral change in the vicinity of the surface trace of the SNAF, which is the most prominent expression of the southern branch of the NAFZ in our model. *Frederiksen et al.* [2015] also observe a change in P-S velocity ratio across the southern NAFZ and attribute it to differences in crustal composition between the Sakarya Zone and the Armutlu Block. Our S wave velocity profiles (Fig. 5) show diffuse relatively low velocities beneath the SNAF clearly terminating at or above Moho depth; coupled with findings from autocorrelation and receiver function studies (*Kahraman et al.* [2015] and *Taylor et al.* [2016]), which do not image any truncation in the Moho signal beneath this branch of the fault, and therefore together these results support the hypothesis that the SNAF is rooted in the crust.

Local seismicity recorded in the region (*Altuncu-Poyraz et al.* [2015]) occurs within the relatively low velocity area imaged beneath the SNAF and often within zones of lower $\delta(V_P/V_S)$ (Fig. 6). Historical records (*Ambraseys* [2002]) show that the SNAF has been the source of fewer large (M_S $\geq$6.8) earthquakes compared to the NNAF, the latest of which dates back to the XV century. Moreover, GPS measurements (*Meade et al.* [2002]) report a lower slip rate (5-10 mm/yr) on the SNAF as compared to the NNAF (~25 mm/yr). We therefore interpret our observations, in conjunction with the findings of previous studies, to indicate that the SNAF represents a weak zone within the Sakarya crust that most likely localises deformation caused by local rotation of the Armutlu and/or Almacik Blocks as central Anatolia extrudes (e.g. *England et al.* [2016]).

4.3 Juxtaposed terrains

Our new S wave velocity and derivative $\delta(V_P/V_S)$ models show clear first-order differences in lithosphere velocity characteristics between the Istanbul Zone, Armutlu Block and Sakarya Zone. We show that the Sakarya Zone typically exhibits relatively low velocities and relatively high $\delta(V_P/V_S)$, in contrast to the Istanbul Zone, which is typically characterised by relatively high velocities and low $\delta(V_P/V_S)$. Between them, the Armutlu Block appears more complex, with both fast and slow velocities and varying $\delta(V_P/V_S)$.

We estimate likely V_P/V_S ranges (at 400 MPa) of the terranes separated by the NNAF to be 1.76-1.82 (south) and 1.71-1.73 (north) using values published by *Christensen* [1996] and hence find that a 4-5 % range in $\delta(V_P/V_S)$ would be reasonable to expect. We therefore conclude that the sharp $\delta(V_P/V_S)$ contrast (and, to a lesser extent, velocity contrast) observed in connection with the NNAF can be explained by the juxtaposition of two distinct terrains: a Triassic-Cretaceous tectonic assemblage in the Armutlu Peninsula (*Yılmaz et al.* [1997]) and sedimentary sequences of Ordovician to Carboniferous age overlaying a Proterozoic granitic and metamorphic basement in the Istanbul Zone (*Görür et al.* [1997]; *Chen et al.* [2002]). We interpret the higher velocity region in the Armutlu block (Fig. 5) to represent the steeply dipping thrusts of mafic and ultramafic rocks, interpreted as the detached basement of the Sakarya Zone upthrusted during the late stages of the Paleotethys closure by Bozkurt et al. (2012). This is consistent with the fact that mafic and ultramafic rocks typically exhibit fast S wave velocities (>3.7 km/s) within the crust (*Christensen* [1996]).

The Istanbul Zone shows relatively high velocities throughout the crust and upper mantle in our P and S velocity models (Fig. 6a-d). A relatively low $\delta(V_P/V_S)$ ratio is also consistent with local earthquake tomography results (*Koulakov et al.* [2010]). Furthermore magnetotelluric observations (*Tank et al.* [2005]) constrain a strong resistor 10 km beneath the Istanbul Zone and gravity studies indicate that the Istanbul Zone is anomalously dense (*Ates et al.* [1999]). We use these results together to interpret that the Istanbul Zone represents an ancient and strong (e.g. *Tesauro et al.* [2007]) terrain with a possibly limited fluid content.

Geological evidence shows that the Sakarya terrain to the south is comprised of a lower Jurassic-Eocene sequence overlying a series of subduction-accretionary units (*Okay and Tüysüz* [1999]; *Şengör and Yilmaz* [1981]) and a high grade metamorphic crystalline basement (*Okay et al.* [2006]). While our $\delta(V_P/V_S)$ values are consistent with estimates for high grade metamorphic facies from *Christensen* [1996], our S and P wave velocity model (Figs. 6a-c) show diffuse low velocities in the Sakarya Zone, which would be compatible with the presence of serpentinite. However, the presence of some ophiolites in the area does not entirely justify these results, suggesting that the composition of the Sakarya Zone may be more complex.

5 Discussion

We discuss the results of the present study, combined with previous P wave teleseismic tomography results (*Papaleo et al.* [2017]) and results from several other studies in the area, in terms of overall fault properties and structure from crust to upper mantle.

5.1 North Anatolian Fault

A number of geophysical studies have been conducted on the North Anatolian fault in an attempt to better characterise its properties and structure, largely motivated by its seismic activity in the past 80 years (*Stein et al.* [1997]). Receiver function studies of the Anatolian peninsula are in agreement on a thinning of the crust from east to west (from ~45 km to ~30 km), compatible with the extensional regime predominant in western Anatolia (*Vanacore* [2013]; *Kind et al.* [2015]); any signature of the NAFZ at Moho depth is, however, not detected in these regional studies.

Low velocities associated with the NAFZ in the crust are found both to the west and east of our study area (*Yolsal-Çevikbilen et al.* [2012]; *Karabulut et al.* [2003]), as well as beneath the NNAF (*Koulakov et al.* [2010]). V_P/V_S results from *Koulakov et al.* [2010], show higher V_P/V_S values of 1.78-1.80 in the vicinity of the NNAF, while to the east the NAFZ seems to be associated with either high or low V_P/V_S values (*Yolsal-Çevikbilen et al.* [2012]), which the authors interpret as a result of variable presence of fluids along the fault zone. Through our $\delta(V_P/V_S)$ results on the other hand, rather than higher or lower $\delta(V_P/V_S)$ beneath the fault, we image the NNAF as a boundary between relatively high $\delta(V_P/V_S)$ to the south and relatively low $\delta(V_P/V_S)$ to the north; while this is compatible with the observed surface geology, we note that our $\delta(V_P/V_S)$ resolution is not as high as the aforementioned studies and therefore might not be able to resolve smaller scale changes beneath the NAFZ.

Pn tomography studies show a change in Pn velocities across the NAFZ (*Mutlu and Karabulut* [2011]; *Gans et al.* [2009]), which correlates well with the P-wave velocity model of *Biryol et al.* [2011] and highlights a difference in velocity north and south of NAFZ. This velocity pattern is also observed in recent P-wave tomography (*Papaleo et al.* [2017]) and the current S-wave tomography study, and most likely reflects the presence of markedly different terrains (i.e. the Istanbul Zone and Sakarya Zone) north and south of the NAFZ.

A key feature in our model is the relatively low velocity anomaly beneath the NNAF, which extends from the crust to the upper mantle. Results showing linked low velocity anomalies in the crust and upper mantle east of 32° longitude (i.e. east of our study area), have been documented by *Fichtner et al.* [2013], and interpreted as a pre-existing zone of weakness (mostly following the boundary between Pontides and Anatolides) that subsequently facilitated the development of a large continuous fault zone. We suggest that our results complement the previous findings and indicate that the NNAF in our study region has a similar structure to the NAFZ to the east, while the SNAF is rooted in the crust. In western Anatolia the pull exerted by subduction along the Hellenic arc is the predominant tectonic force in the region, exerting control over the extrusion velocity of the Anatolian peninsula (*Flerit et al.* [2004]) and, as indicated by the GPS vector field (*Reilinger* *et al.* [2006]), causing the rotation of the extruding plate. While the NNAF propagates in the Sea of Marmara as a single throughgoing dexteral strike-slip fault (*Le Pichon et al.* [2001]), the propagation of the SNAF is less clear, suggesting that this branch of the fault might have been formed to accommodate the rotation of the Almacik and Armutlu blocks within the Anatolian plate (*England et al.* [2016]).

5.2 Comparison with other major fault zones

Low velocities related to the presence of major strike slip faults have been documented, for example, beneath the Alpine Fault (*Smith et al.* [1995]), San Andreas Fault (*Thurber et al.* [2004]) and Altyn Tagh (*Wittlinger et al.* [1998]; *Zhao et al.* [2006]). Geophysical images of the Alpine Fault show that it is likely to be <10 km wide in the crust and <30 km wide in the uppermost mantle (almost identical to our observations in this study), with a possible crustal decollement (e.g. *Stern et al.* [2007]), while seismic and magnetotelluric data typically shows a steeply dipping <5 km wide fault zone beneath the San Andreas fault that extends in the lower crust and may widen to <25 km as it passes into the upper mantle (e.g. *Fuis and Clowes* [1993]; *Becken et al.* [2008]).

The possible downward continuation of major strike slip faults in the upper mantle has also been debated (e.g. *Wittlinger et al.* [2004]; *Zhao et al.* [2006]; *Fuis et al.* [2007]); however, several studies point to the presence of shear zones beneath major faults. *Wittlinger et al.* [1998] image a low velocity zone of ~40 km width in the upper mantle beneath the Altyn Tagh fault that they interpret as a shear zone; this result, also supported by a shear wave splitting study by *Herquel et al.* [2004], is comparable to our observation, which hints at the presence of a ~30 km wide shear zone beneath the NNAF. Estimates for the San Andreas fault on the other hand range from a ~50 km shear zone (*Ford et al.* [2014]) to a broader, ~130 km wide, zone of shear in the upper mantle (*Titus et al.* [2007]), more similar to what has been observed in New Zealand (*Audoine et al.* [2000]; *Wilson et al.* [2004]). Interestingly, as has been observed by *Molnar and Dayem* [2010], all of these faults appear to be bounded by a stronger block to one side and a deforming block on the other side, perhaps suggesting that the presence of heterogeneous lithosphere may favour the formation of strike slip faults.

5.3 Fault zone width throughout the lithosphere

Field observations of exhumed fault zones report the presence of mylonite belts of up to 30 km width in the lower crust, which narrow significantly upward (e.g. *Hanmer* [1988]; *Vauchez and Tommasi* [2003] and references therein), and suggesting that shear zone width narrows with decreasing temperature and depth (*Burgmann and Dresen* [2008]). This is broadly consistent with the results of our study, where we find that the relatively low velocity anomalies associated with the NNAF tend to widen with depth. However, we note that rather than an approximately smooth width variation with depth as predicted by previous models, we observe a step-like change in width at lower crustal depth, suggesting that other variables may play an important role in determining the evolution of fault zone width with depth.

Platt and Behr [2011] argue that shear zone width depends on the interplay between the effects of deformation mechanisms, temperature increase and stress decrease with depth. In particular, they find that upper mantle fault zone width is lowest in strong, dry, cratonic crust and that below the seismogenic layer fault zone width could reach up to 180 km for a San Andreas type fault. According to their model, the width of a shear zone is directly proportional to the plate velocity which, in their calculation, they assume to be ~50 mm/yr. In the case of the NNAF (assuming similar lithologies for both faults), the average velocity is ~25 mm/yr (*Meade et al.* [2002]), implying a fault width of up to 90 km. This estimate is large compared to our results, showing an average shear zone width of 30 km in the uppermost mantle. However, this could be explained either by the potentially invalid assumption of similar lithologies between the two faults or, partly, by taking into account the resolution limits in our model.

Looking at approximately 90 years of fault deformation data, *Kenner and Segall* [2003] showed that the best fitting model for fault zones incorporates a weak vertical shear zone in the crust beneath major faults, which is in accordance with results from *Yamasaki et al.* [2014], who find that the NAFZ can be modelled as a vertical weak zone extending to mid-crustal depth. In addition, *Yamasaki et al.* [2014] indicated that the best fitting model for the NAFZ is that of a sharp weak zone boundary, implying that the weak zone (i.e. the NAFZ) may be bounded by a relatively abrupt change in material properties (e.g. lithological contrast, grain size reduction, water content), consistent with the presence of different terranes to the north and south of the NAFZ.

6 Conclusions

We have presented results from S wave teleseismic tomography and $\delta(V_P/V_S)$ models obtained from the recordings of a dense array of seismic stations in western Anatolia and show that SNAF and NNAF exhibit very different characteristics.

Through our results we are able to constrain the width and extent of the NNAF in both crust and upper mantle. In the upper crust the NNAF appears to localise deformation in a narrow corridor <10 km wide, which widens -in a sharp rather than smoothly varying manner- to ~30 km in the lower crust; the low velocities continuing from lower crust to upper mantle support the idea of a shear zone associated with the northern branch of the fault, whose width in the upper mantle we constrain to be ≤50 km. In this context, our observations support the hypothesis that the NNAF is a narrow fault zone, separating a stronger block (Istanbul Zone) to the north from a deforming block (Armutlu - Sakarya Zone) to the south, a feature that has been observed in most major strike-slip faults (*Molnar and Dayem* [2010]).In addition, our results suggest that the structure of the northern branch of the NAFZ is similar to the structure of the NAFZ east of 32°, as imaged with full waveform inversion (*Fichtner et al.* [2013]).

The SNAF does not have a very strong signal in our velocity model and $\delta(V_P/V_S)$ results, showing a 2% $\delta(V_P/V_S)$ change beneath the surface trace of the southern branch of the fault, is the clearest expression of the SNAF. The clear change in the velocity pattern beneath the fault at Moho depth together with results from other studies, however, support the hypothesis that the SNAF is likely rooted in the crust, accommodating the rotation of the Armutlu and Almacik Blocks.

Acknowledgments

DANA (Dense Array for Northern Anatolia) is part of the Faultlab project, a collaborative effort by the University of Leeds, Boğaziçi University Kandilli Observatory and Earthquake Research Institute (BU-KOERI) and Sakarya University. Major funding was provided by the UK Natural Environment Research Council (NERC) under grant NE/I028017/1. Equipment was provided and supported by the NERC Geophysical Equipment Facility (SEIS-UK). This project is also supported by Boğaziçi University Scientific Research Projects (BAP) under grant 6922 and Turkish State Planning Organization (DPT) under the TAM project, number 2007K120610. We are indebted to the Faultlab seismological fieldwork team members Sebastian Rost, Greg Houseman, David Thompson, Sandra Karl, Luke Jackson, Hannah Bentham, Ekbal Hussain, Selda Altuncu Poyraz, Uğur Teoman, Niyazi Türkelli, Metin Kahraman, Murat Utkucu, Levent Gülen. Victoria Lane (SEIS-UK) provided invaluable technical and practical seismological assistance. DANA seismological data (DANA, 2012) can be accessed via the IRIS website (www.iris.edu).

References

Akbayram, K., Sorlien, C., and Okay, A. I. (2016), Evidence of a minimum 52 ± 1 km of total offset along the northern branch of the North Anatolian Fault in northwest Turkey, *Tectonophysics*, *668-669*, 35–41.

Allam, A. A., and Ben-Zion, Y. (2012), Seismic velocity structures in the southern California plate boundary environment from double-difference tomography, *Geophys. J. Int.*, *190*, 1181–1196.

Altuncu Poyraz, S., Teoman, M. U., Türkelli, N., Kahraman, M., Cambaz, D., Mutlu, A., Rost. S., Houseman, G. A., Thompson, D. A., Cornwell, D. G., Utkucu, M., and Gülen, L. (2015), New constraints on micro-seismicity and stress state in the western part of the North Anatolian Fault Zone: Observations from a dense seismic array, *Tectonophysics*, *656*, 190–201.

Ambraseys, N. (2002), The seismic activity of the Marmara Sea region over the past 2000 years, *Bull. Seismol. Soc. Am.*, *92*, 1–18.

Ates, A., Kearey, P., and Tufan, S. (1999), New gravity and magnetic maps of Turkey, *Geophys. J. Int. Research Note*, *136*, 499–502.

Audoine, E., Savage, M. K., and Gledhill, K. (2000), Seismic anisotropy from local earthquakes in the transition region from a subduction to a strike-slip plate boundary, New Zealand, *J. Geophys. Res.*, *105*, 8013–8033.

Becken, M., Ritter, O., Park, S. K., Bedrosian, P. A., and Weckmann, U. (2008), A deep crustal fluid channel into the San Andreas fault system near Parkfield, California, *Geophys. J. Int.*, *173*, 718–732.

Beyhan, G., and Alkan, M. A. (2015), Three dimensional structure of Vp in the upper crust of the Sakarya Basin, NW Turkey, *Arab J. Geosci.*, *8*, 6371–6383.

Biryol, C. B., Beck, S. L., Zandt, G., and Özacar A. A. (2011), Segmented African lithosphere beneath the Anatolian region inferred from teleseismic P-wave tomography, *Geophys. J. Int. 184*, 1037–1057.

Bozkurt, E., Winchester, J. A., Satir, M., Crowley, Q. G., and Ottley, C. J. (2013), The Almacik mafic-ultramafic complex: exhumed Sakarya subcrustal mantle adjacent to the Istanbul Zone, NW Turkey, *Geol. Mag.*, *150*, 254–282.

Brisbourne, A. (2012), How to store and share geophysical data, *Astronomy and Geophysics*, *53*, 19–20.

Bulut, F., Ben-Zion, Y., and Bonhoff, M. (2012), Evidence for a bimaterial interface along the Mudurnu segment of the North Anatolian Fault Zone from polarization analysis of P waves, *Earth Plan. Sci. Lett.*, *327-328*, 17–22.

Burgmann, R., and Dresen, G. (2008), Rheology of the lower crust and upper mantle: evidence from rock mechanics, geodesy and field observations, *Annu. Rev. Earth Planet. Sci.*, *36*, 531–567.

Chen, F., Siebel, W., Satir, M., Terzioğlu, and Saka, K. (2002), Geochronology of the Karadere basement (NW Turkey) and implication for the geological evolution of the Istanbul Zone, *Int. J. Earth Sci.*, *91*, 469–481.

Christensen, N. I. (1996), Poisson's ratio and crustal seismology, *J. Geophys. Res.*, *101*, 3139–3156.

DANA (2012), *Dense array for Northern Anatolia*, doi:10.7914/SN/YH_2012, Other/Seismic Network

Eberart-Phillips, D., Reyners, M., Chadwick, M., and Chiu, J.-M. (2005), Crustal heterogeneitis and subduction processes: 3D Vp, Vp/Vs and Q in the southern North Island, New Zealand, *Geophys. J. Int.*, *162*, 270–288.

England, P., Houseman, G., and Nocquet, J.-M. (2016), Constraints from GPS measurements on the dynamics of deformation in Anatolia and the Aegean, *J. Geophys. Res. Solid Earth*, *121*, 8888–8916.

Fichtner, A., Saygin, E., Taymaz, T., Cupillard, P., and Capdeville, Y. (2013), The deep structure of the North Anatolian Fault Zone, *Earth Plan. Sci. Lett.*, *373*, 109–117.

Flerit, F., Armijo, R., King, G., and Meyer, B. (2004), The mechanical interaction between the propagating North Anatolian Fault and the back-arc extension in the Aegean, *Earth Plan. Sci. Lett.*, *224*, 347–362.

Ford, H. A., Fischer, K. M., and Lekic, V. (2014), Localized shear in the deep lithosphere beneath the San Andreas fault system, *Geology*, *42*, 295–298.

Frederiksen, A. W., Thompson, D. A., Rost, S., Cornwell, D. G., Gülen, L., Houseman, G. A., Kahraman, M., Altuncu Poyraz, S., Teoman, U. M., Türkelli, N., and Utkucu,

M. (2015), Crustal thickness variations and isostatic disequilibrium across the North Anatolian Fault, western Turkey, *Geophys. Res. Lett.*, *42*, 751–757.

Fuis., G. S., and Clowes, W. D. (1993), Comparison of deep structure along three transects of the western North American margin, *Tectonics*, *12*, 1420–1435.

Fuis, G. S., Kohler, M. D., Scherwath, M., Brink, U., Van Avendonk, H. J. A., and Murphy, J. M. (2007), A comparison between the transpressional plate boundaries of South Island, New Zealand, and southern California, USA: the Alpine and San Andreas fault systems, *A continental plate boundary: Tectonics at South Island, New Zealand*.

Gans, C. R., Beck, S. L., Zandt, G., Biryol, C. B., and Ozacar, A. A. (2009), Detecting the limit of slab break-off in central Turkey: new high-resolution Pn tomography results, *Geophys. J. Int.*, *179*, 1566–1572.

Görür, N., Monod, O., Okay, A. I., Şengör, A. M. C., Tüysüz, O., Yiğitbaş, E., Sakinç, M., and Akkök, R. (1997), Palaeogeographic and tectonic position of the Carboniferous rocks of the western Pontides (Turkey) in the frame of the Variscan belt, *Bulletin SocietÃl' Geologique de France*, *168*, 197–205.

Hammond, W. C., and Toomey, D. R. (2003), Seismic velocity and anisotropy heterogeneity beneath the Mantle Electromagnetic and Tomography Experiment (MELT) region of the East Pacific Rise from analysis of P and S body waves, *J. Geophys. Res.*, *108*.

Hanmer, S. (1988), Great Slave Lake Shear Zone, Canadian Shield: reconstructed vertical profile of a crustal-scale fault zone, *Tectonophysics*, *149*, 245–264.

Herquel, G., Tapponnier, P., Wittlinger, G., Mei, J., and Danian, S. (2004), Teleseismic shear wave splitting and lithospheric anisotropy beneath and across the Altyn Tagh fault, *Geophys. Res. Lett.*, *26*, 3525–3528.

Hong, T.-K., and Menke, W. (2006), Tomographic investigation of the wear along the San Jacinto fault, southern California, *Phys. Earth Plan. Int.*, *155*, 236–248.

Kahraman, M., Cornwell, D. G., Thompson, D. A., Rost, S., Houseman, G. A., Türkelli, N., Teoman, U., Altuncu Poyraz, S., Utkucu, M., Gülen, L. (2015), Crustal-scale shear zones and heterogeneous structure beneath the North Anatolian Fault Zone, Turkey, revealed by a high-density seismometer array, *Earth Plan. Sci. Lett.*, *430*, 129–139.

Karabulut, H., Özalaybey, S., Taymaz, T., Aktar, M., Selvi, O., and Kocaoğlu, A. (2003), A tomographic image of the shallow crustal structure in the eastern Marmara, *Geophys. Res. Lett.*, *30*.

Karahan, A., Berckhemer, H., Baier, B. (2001), Crustal structure at the western end of the North Anatolian Fault Zone from deep seismic sounding, *Ann. Geophys.*, *44*, 49–68.

Kenner, S. J., and Segall P. (2003), Lower crustal structure in northern California: implications from strain-rate variations following the 1906 San Francisco earthquake, *J. Geophys. Res.*, *108*.

Kennett, B. N. L., Sambridge, M., and Williamson, P. R. (1988), Subspace methods for large scale inverse problems involving multiple parameter classes, *Geophys. J. Int.*, *94*, 237–247.

Kind, R., Eken, T., Tilmann, F., Sodoudi, F., Taymaz, T., Bulut, F., Yuan, X., Can, B., and Schneider, F. (2015), Thickness of the lithosphere beneath Turkey and surroundings from S-receiver functions, *Solid Earth*, *6*, 971–984.

Koulakov, I., Bindi, D., Parolai, S., Grosser, H., and Milkereit, C. (2010), Distribution of seismic velocities and attenuation in the crust beneath the North Anatolian Fault (Turkey) from local earthquake tomography, *Bull. Seismol. Soc. Am.*, *100*, 207–224.

Le Pichon, X., Şengör, A. M. C., Dermibağ, E., Rangin, C., İmren, C., Armijo, R., Görür, N., et al. (2001), Te Active Main Marmara Fault, *Earth Plan. Sci. Lett.*, *192*, 595–616.

Le Pichon, X., Şengör, A. M. C., Kende, J., İmren, C., Henry, P., Grall, C., and Karabulut, H. (2016), Propagation of a strike-slip plate boundary within an extensional environment: the westward propagation of the North Anatolian Fault, *Can. J. Earth Sci.*, *53*, 1416–1439.

Lin, F.-C., Ritzwoller, M. H., Yang, Y., Moschetti, M. P., and Fouch, M. J. (2011), Complex and variable crustal and uppermost mantle seismic anisotropy in the western United States, *Nat. Geosci.*, *4*, 55–61.

Lin, G., and Thurber, C. H. (2012), Seismic velocity variations along the rupture zone of the 1989 Loma Prieta earthquake, California, *J. Geophys. Res.*, *117*.

Meade, B. J., Hager, B. H., McClusky, S. C., Reilinger, R. E., Ergintav, S., Lenk, O., Barka, A., and Ozener, H. (2002), Estimates of seismic potential in the Marmara Sea region from block models of secular deformation constrained by global positioning system measurements, *Bull. Seismol. Soc. Am.*, *92*, 208–215.

Molnar, P., and Dayem, K. (2010), Major intracontinental strike-slip faults and contrasts in lithospheric strength, *Geosphere*, *6*, 444–467.

Mutlu, A. K., and Karabulut, H. (2011), Anisotropic Pn tomography of Turkey and adjacent regions, *Geophys. J. Int.*, *187*, 1743–1758.

Najdahmadi, B., Bonhoff, M., and Ben-Zion, Y. (2016), Bimaterial interfaces at the Karadere segment of the North Anatolian Fault, northwest Turkey, *J. Geophys. Res. Solid Earth*, *121*, 931–950.

Norris, R. J., and Toy, V. G. (2014), Continental transforms: A view from the Alpine Fault, *J. Struct. Geol.*, *64*, 3–31.

Okay, A. I., and Tüysüz, O. (1999), Tethyan suture of northern Turkey, *Geol. Soc. Lond. Spec. Publ.*, *156*, 475–515.

Okay, A. I., Satir, M., and Siebel, W. (2006), Pre-Alpide orogenic events in the Eastern Mediterranean region, *Geol. Soc. Lond. Memoirs*, *32*, 389–405.

Özeren, M. S., and Holt, W. E. (2010), The dynamics of eastern Mediterranean and eastern Turkey, *Geophys. J. Int.*, *183*, 1165–1184.

Papaleo, E., Cornwell, D. G., and Rawlinson, N. (2017), Seismic tomography of the North Anatolian Fault: New insights into structural heterogeneity along a continental strike-slip fault, *Geophys. Res. Lett.*, *44*, 2186–2193.

Platt., J. P., and Behr, W. M. (2011), Deep structure of lithospheric fault zones, *Geophys. Res. Lett.*, *38*.

Rawlinson, N., and Kennett, B. L. N. (2004), Rapid estimation of relative and absolute delay times across a network by adaptive stacking, *Geophys. J. Int*, *157*, 332–340.

Rawlinson, N., Reading, A. M., and Kennett, B. L. N. (2006), Lithospheric structure of Tasmania from a novel form of teleseismic tomography, *J. Geophys. Res.*, *111*.

Reilinger, R., McClusky, S., Vernant, P., Lawrence, S., Ergintav, S., Cakmak, R., Ozener, H., Kadirov, F., Guliev, I., Stepanyan, R., Nadariya, M., Hahubia, G., Mahmoud, S., Sakr, K., ArRajehi, A., Paradissis, D., Al-Aydrus, A., Prilepin, M., Guseva, T., Evren, E., Dmitrotsa, A., Filikov, S. V., Gomez, F., Al-Ghazzi, R., and Karam, G. (2006), GPS constraints on continental deformation in the Africa-Arabia-Eurasia continental collision zone and implications for the dynamics of plate interactions, *J. Geophys. Res. Solid Earth*, *111*.

Şengör, A. M. C. and Yilmaz, Y. (1981), Tethyan evolution of Turkey: a plate tectonic approach, *Tectonophysics*, *75*, 181–141.

Şengör, A. M. C., Tüysüz, O., İmren, C., Sakınç, M., Eyidoğan, H., Görür, N., Le Pichon, X., and Rangin, C. (2005), The North Anatolian Fault: a new look, *Annu. Rev. Earth. Planet. Sci.*, *33*, 37–112.

Schmandt, B., and Humphreys, E. (2010), Complex subduction and small-scale convection revealed by body-wave tomography of the western United States upper mantle, *Earth Plan. Sci. Lett.*, *297*, 435–445.

Sethian, J. A. (1999), Fast marching methods, *SIAM Rev.*, *41*, 199–235.

Sibson R. H. (1983), Continental fault structure and the shallow earthquake source, *J. Geol. Soc. London*, *140*, 741–767.

Smith, E. G. C., Stern, T., and O'Brien, B. (1995), A seismic velocity profile across the central South Island, New Zealand, from explosion data, *New Zealand Journal of Geology and Geophysics*, *38*, 565–570.

Stein, R. S., Barka, A. A., and Dieterich, J. H. (1997), Progressive failure on the North Anatolian fault since 1939 by earthquake stress triggering, *Geophys. J. Int.*, *128*, 594–604.

Stern, T. A., Okaya, D., Kleffmann, S., Scherwath, M., Henrys, S., and Davey, F. (2007), Geophysical exploration of the Alpine Fault Zone, *A continental plate boundary: tectonics of South Island, New Zealand*, *AGU Geophysical Monograph*, *175*, 209–236.

Tank, S. B., Honkura, Y., Ogawa, Y., Matsushima, M., Oshiman, N., Tunçer, M. K., Çelik, C., Tolak, E., and Işikara, M. (2005), Magnetotelluric imaging of the fault rupture area of the 1999 İzmit (Turkey) earthquake, *Phys. Earth Plan. Int.*, *150*, 213–225.

Taylor, G., Rost, S., and Houseman, G. A. (2016), Crustal imaging across the North Anatolian Fault Zone from the autocorrelation of ambient seismic noise, *Geophys. Res. Lett.*, *43*, 2502–2507.

Tesauro, M., Kaban, M. K., Cloetingh, S. A. P. L., Hardebol, N. J., and Beekman, F. (2007), 3D strength and gravity anomalies of the european lithosphere, *Earth Plan. Sci. Lett.*, *263*, 56–73.

Thurber, C., Roecker, S., Zhang, H., Baher, S., and Ellsworth, W. (2004), Fine-scale structure of the San Andreas fault zone and location of the SAFOD target earthquakes, *Geophys. Res. Lett.*, *31*.

Titus, S. J., Medaris, L. G., Wang, H. F., and Tikoff, B. (2007), Continuation of the San Andreas fault system into the upper mantle: evidence from spinel peridotite xenoliths in the Coyote Lake basalt, central California, *Tectonophysics*, *429*, 1–20.

Vanacore, E. A., Taymaz, T., and Saygin, E. (2013), Moho structure of the Anatolian Plate from receiver function analysis, *Geophys. J. Int.*, *193*, 329–337.

Vauchez, A., and Tommasi, A. (2003), Wrench faults down to the astenosphere: Geological and geophysical evidence and termo-mechanical effects, *Geol. Soc. Lond., Spec. Publ.*, *210*, 15–34.

Wilson, C. K., Jones, C. H., Molnar, P., Sheehan, A. F., and Boyd, O. S. (2004), Distributed deformation in the lower crust and upper mantle beneath a continental strike-slip fault zone: Marlborough fault system, South Island, New Zealand, *Geology*, *32*.

Wittlinger, G., Tapponnier, P., Poupinet, G., Mei, J., Danian, S., Herquel, G. and Masson, F. (1998), Tomographic evidence for localized lithospheric shear along the Altyn Tagh fault, *Science*, *282*, 74–76.

Wittlinger, G., Vergne, J., Tapponnier, P., Farra, V., Poupinet, M. J., Su, H., Herquel, G., and Paul, A. (2004), Teleseismic imaging of subducting lithosphere and Moho offsets beneath western Tibet, *Earth Plan. Sci. Lett.*, *221*, 117–130.

Yamasaki, T., Wright, T. J., and Houseman, G. A. (2014), Weak ductile shear zone beneath a major strike-slip fault: inferences from earthquake cycle model constrained by geodetic observations of the western North Anatolian Fault Zone, *J. Geophys. Res. Solid Earth*, *119*, 3678–3699.

Yılmaz, Y., Tüysüz, O., Yiğitbas, E., Genç, Ş. C., and Şengör, A. M. C. (1997), Geology and tectonic evolution of the Pontides, *Regional and petroleum geology of the Black Sea and surrounding region: AAPG Memoir*, *68*, 183–226.

Yolsal-Çevikbilen, S., Berk Biryol, C., Beck, S., Zandt, G., Taymaz, T., Adiyaman, H. E., and Arda Özacar, A. (2012), 3-D crustal structure along the North Anatolian Fault in north-central Anatolia revealed by local earthquake tomography, *Geophys. J. Int.*, *188*, 819–849.

Zhao, J., Mooney, W. D., Zhang, X., Li, Z., Jin, Z., and Okaya, N. (2006), Crustal Structure across the Altyn Tagh Range at the northern margin of the Tibetan plateau and tectonic implications, *Earth Plan. Sci. Lett.*, *241*, 804–814.

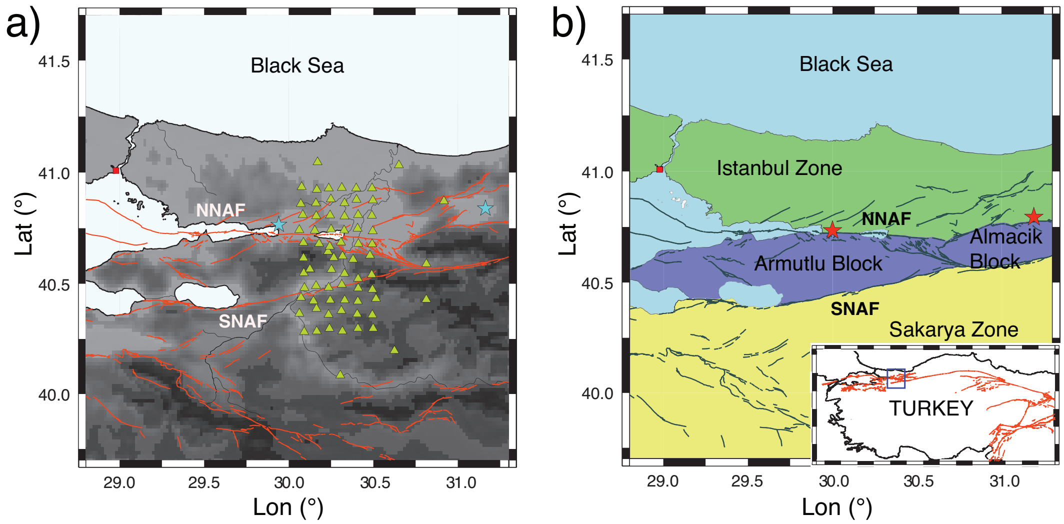

Figure 1. a) Relief map of the study area with station locations (green triangles) and surface fault traces (red lines). The red square marks the position of Istanbul, while the two blue stars indicate the epicentres of the 1999 Izmit and Düzce events. b) Map highligting the three main geological units in the area, bounded by the two strands of the North Anatolian Fault: the Istanbul Zone, the Armutlu and Almacık Blocks and the Sakarya Zone. The inset shows the location of the study.

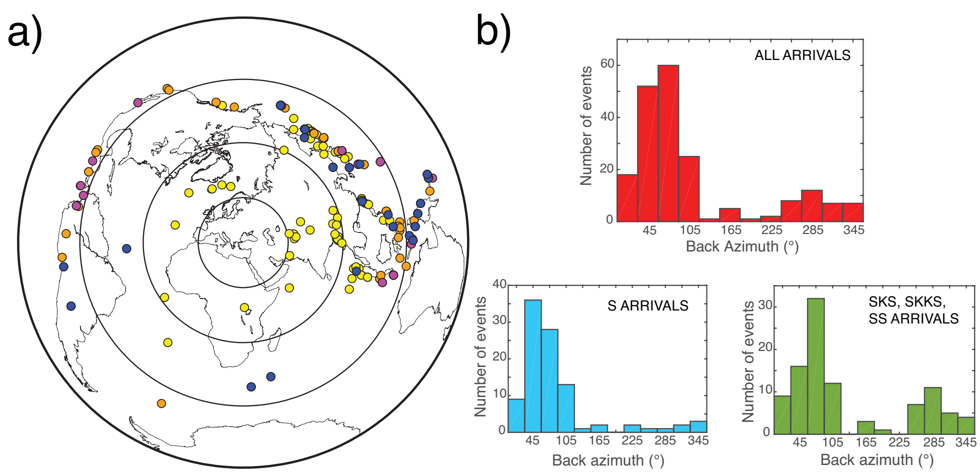

Figure 2. a) Locations of the events used for S wave teleseismic tomography. Yellow dots represent earthquakes of $m_b \geq 5.5$ from which direct S-arrivals are extracted; orange dots are earthquakes from which SKS arrivals are extracted; purple dots represent earthquakes from which SS arrivals are extracted and blue dots represent earthquakes from which SKKS arrivals are extracted. Black concentric circles represent 30° contours in angular distance from the centre of the array. b) Back azimuth distribution of the sources.

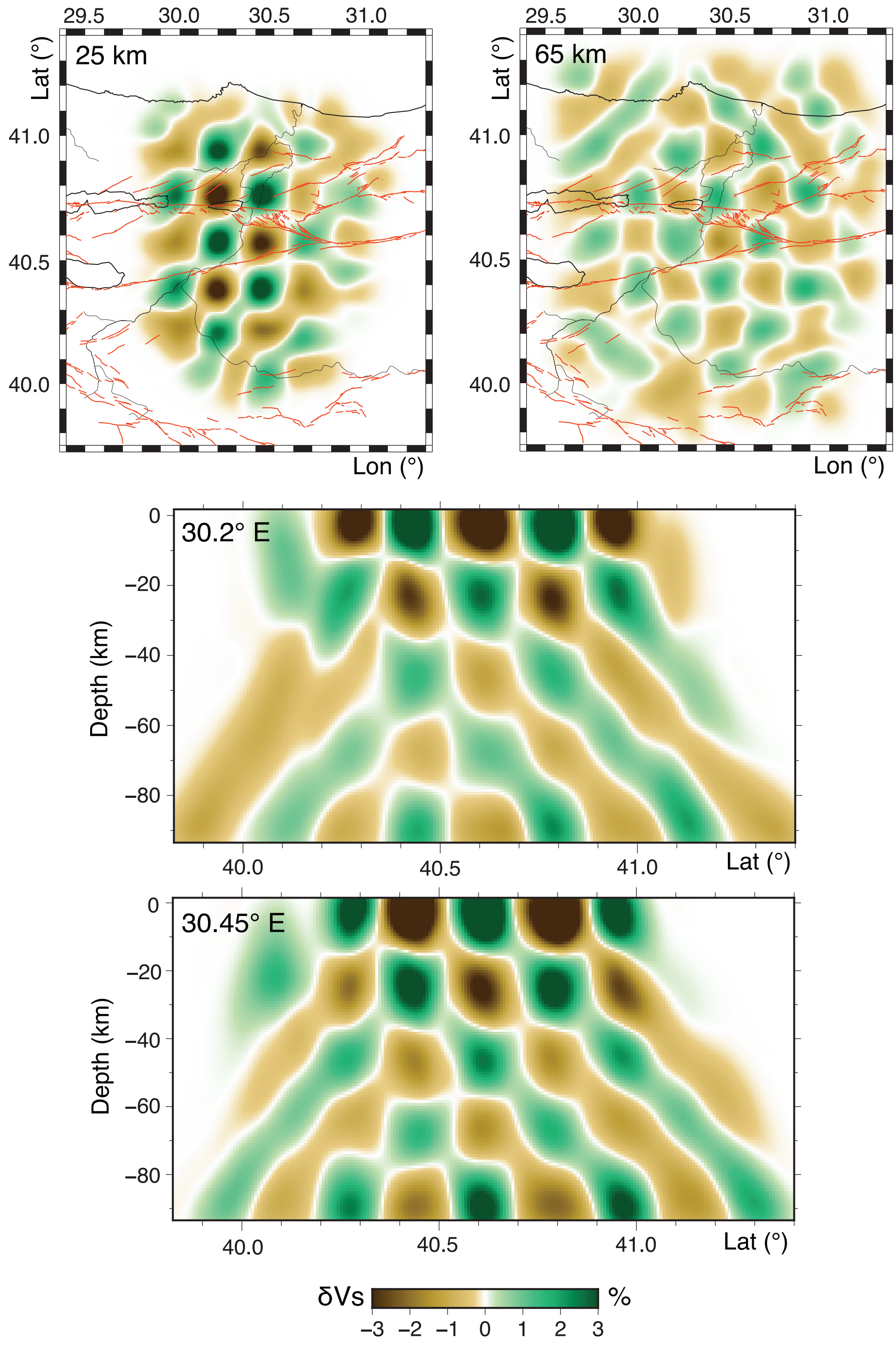

150 **Figure 3.** Results of the S-wave checkerboard test for two depth slices at 25 and 65 km depth and two
151 north-south vertical profiles at 30.2 and 30.45° E; the size of the input anomaly is 15 x 15 x 15 km.

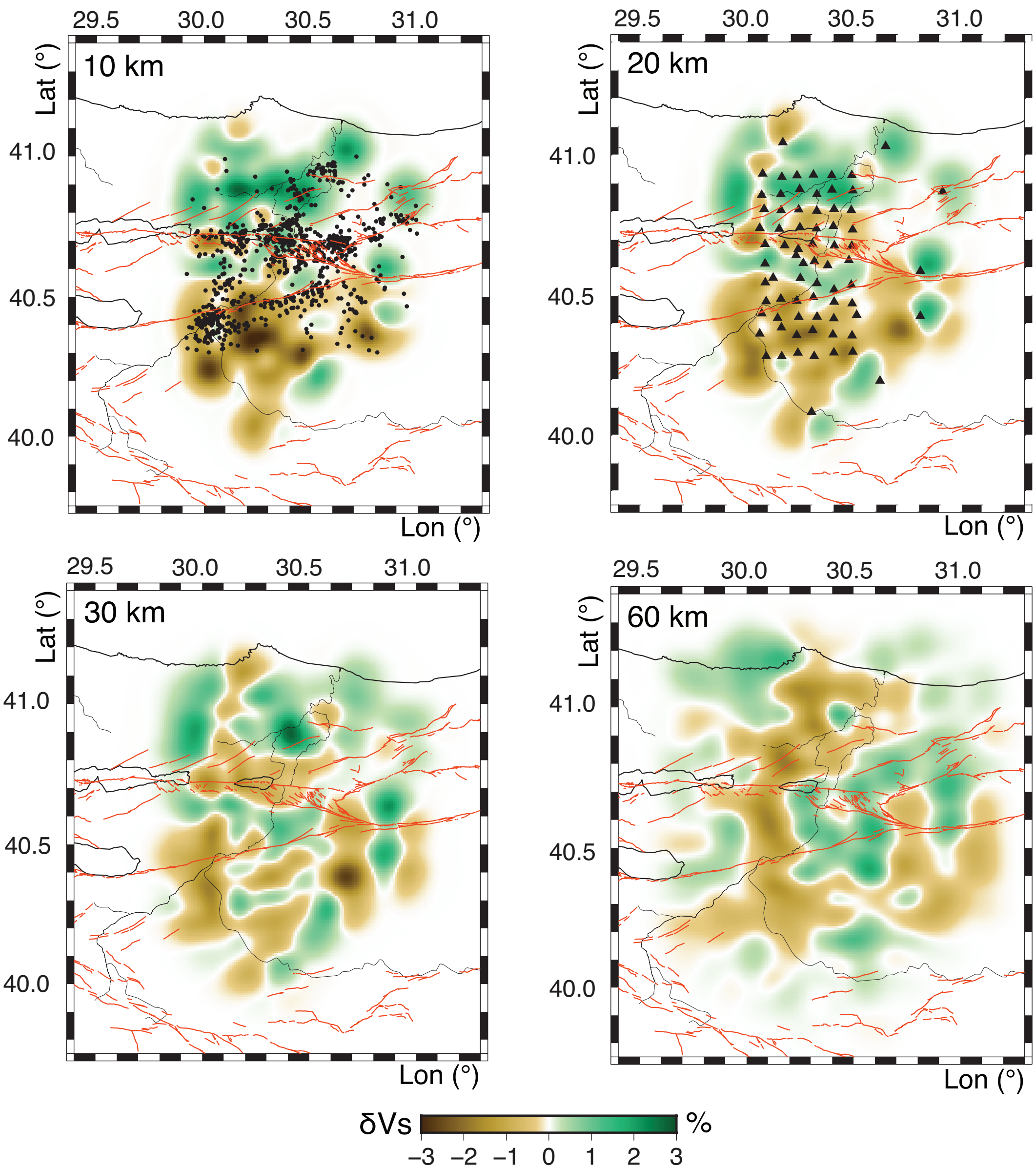

216 **Figure 4.** Depth profiles at 10, 20, 30 and 60 km. The 10 km depth profile (top left) shows the local seismicity recorded during the period of deployment of the DANA array (*Altuncu-Poyraz et al.* [2015]), while the 20 km depth profile (top right) shows the locations of the stations. Surface fault traces are represented by red lines.

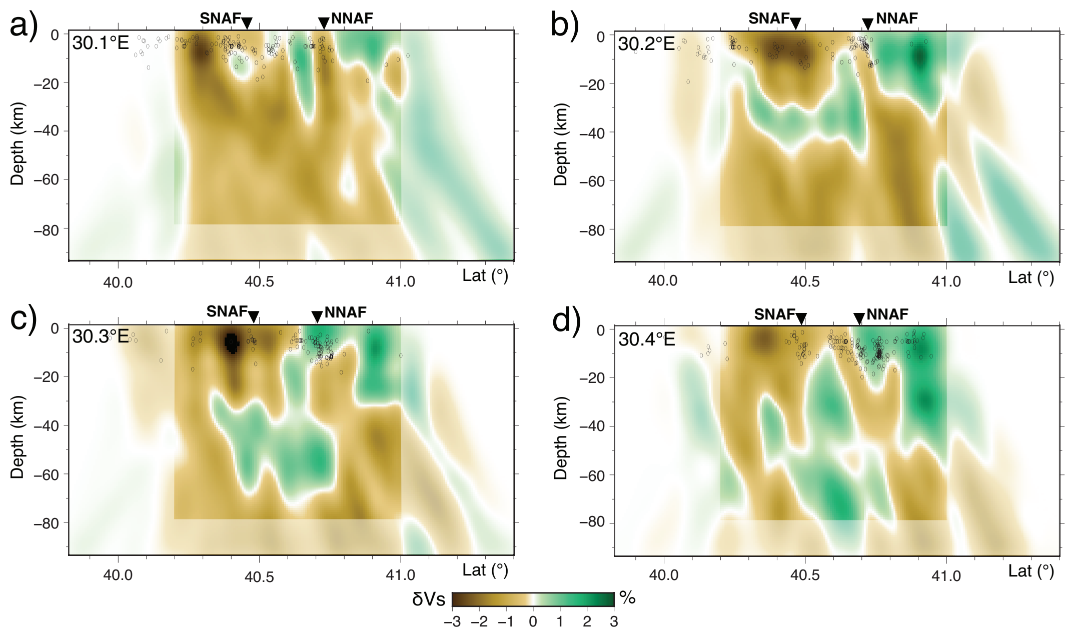

220 **Figure 5.** Vertical profiles through our 3D S-wave velocity model; black dots show the local seismicity
221 within ±0.05° recorded during the deployment period of the DANA array (*Altuncu-Poyraz et al.* [2015]).

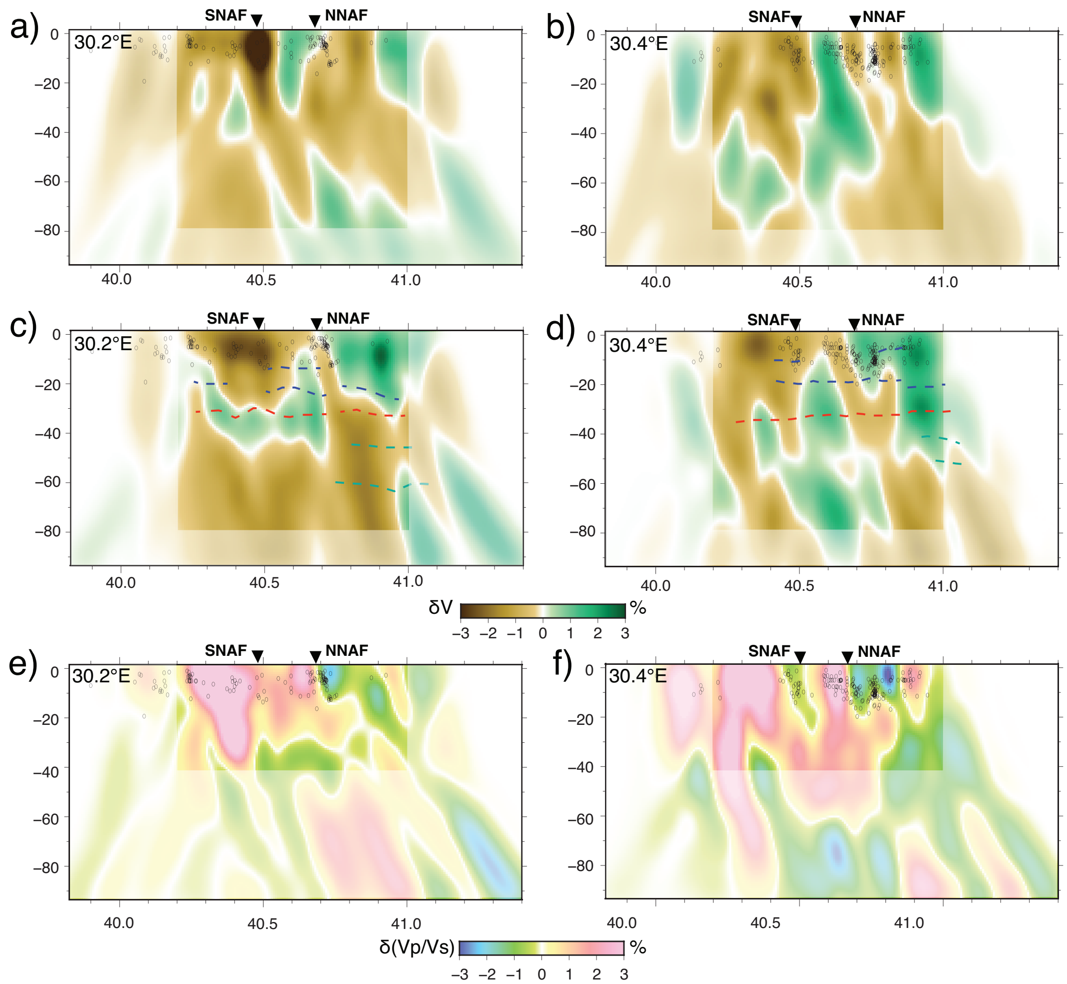

Figure 6. a-b) Vertical north-south profiles through the 3D P-wave velocity model; the grid spacing has been adjusted to match the one used for the S-wave model; black dots show the local earthquakes within ±0.05°, perpendicular to profile, recorded during the deployment period of the DANA array (*Altuncu-Poyraz et al.* [2015]); c-d) Vertical north-south profiles through the 3D S-wave velocity model; black dots show the local earthquakes within ±0.05°, perpendicular to profile; e-f) $\delta(V_P/V_S)$ profiles, also showing the same set of earthquakes to the corresponding plot above.

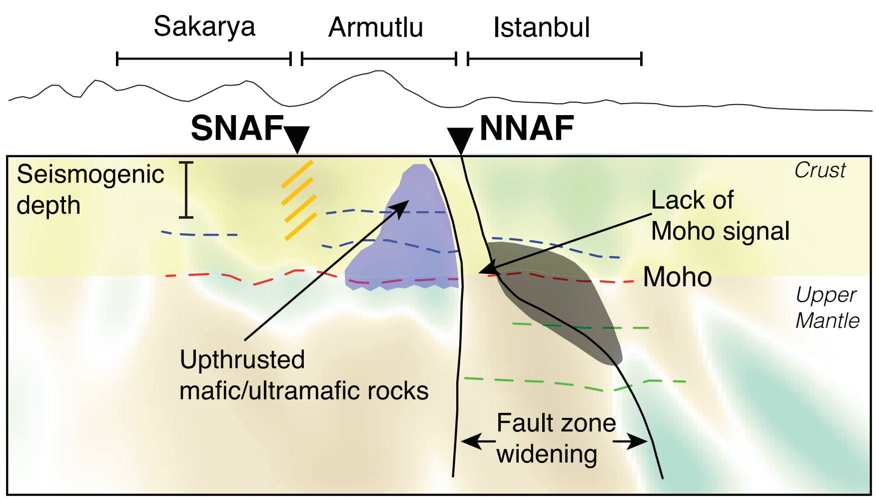

328 **Figure 7.** Schematic interpretation of the structure of the fault. The shadowed area represents the possible
329 variability of the fault shear zone along the profiles, while the yellow lines beneath the SNAF denote the
330 area of influence of the fault as inferred from local seismicity (*Altuncu-Poyraz et al.* [2015]), V_P/V_S results
331 and results from receiver function analysis (*Kahraman et al.* [2015]). Blue, red and green dashed lines are
332 results from receiver function analysis (*Kahraman et al.* [2015]) and represent crustal structures, the Moho
333 and anisotropic layers respectively. The shaded blue area represents the high velocity zone observed between
334 NNAF and SNAF and likely associated with ultramafic rocks upthrusted from the Sakarya Zone (*Bozkurt et*
335 *al.* [2013])

Fig1.

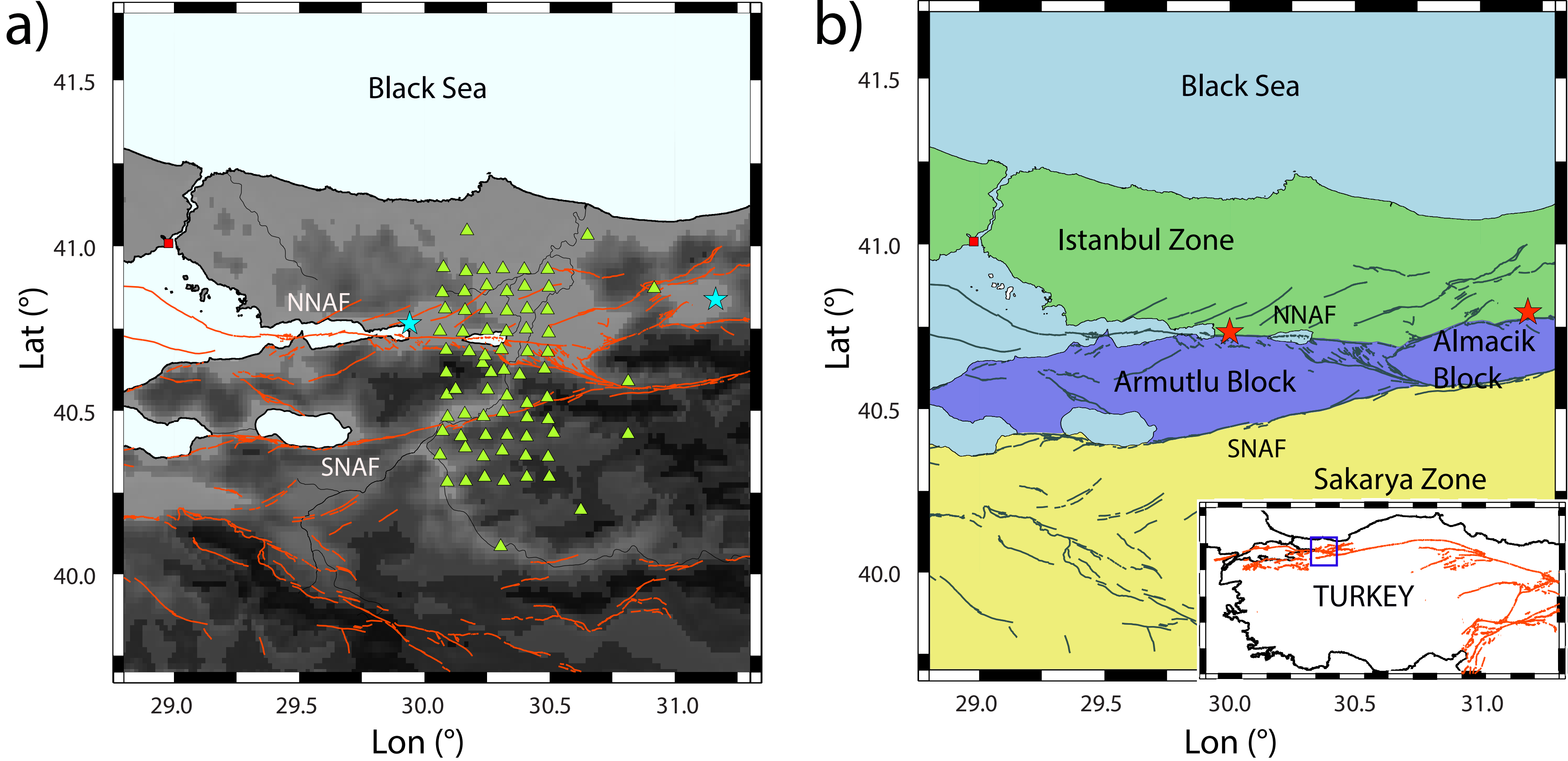

a)
b)
Black Sea
NNAF
SNAF
Istanbul Zone
Armutlu Block
Almacik Block
Sakarya Zone
TURKEY
41.5
41.0
40.5
40.0
29.0
29.5
30.0
30.5
31.0
Lat (°)
Lon (°)

Fig2.

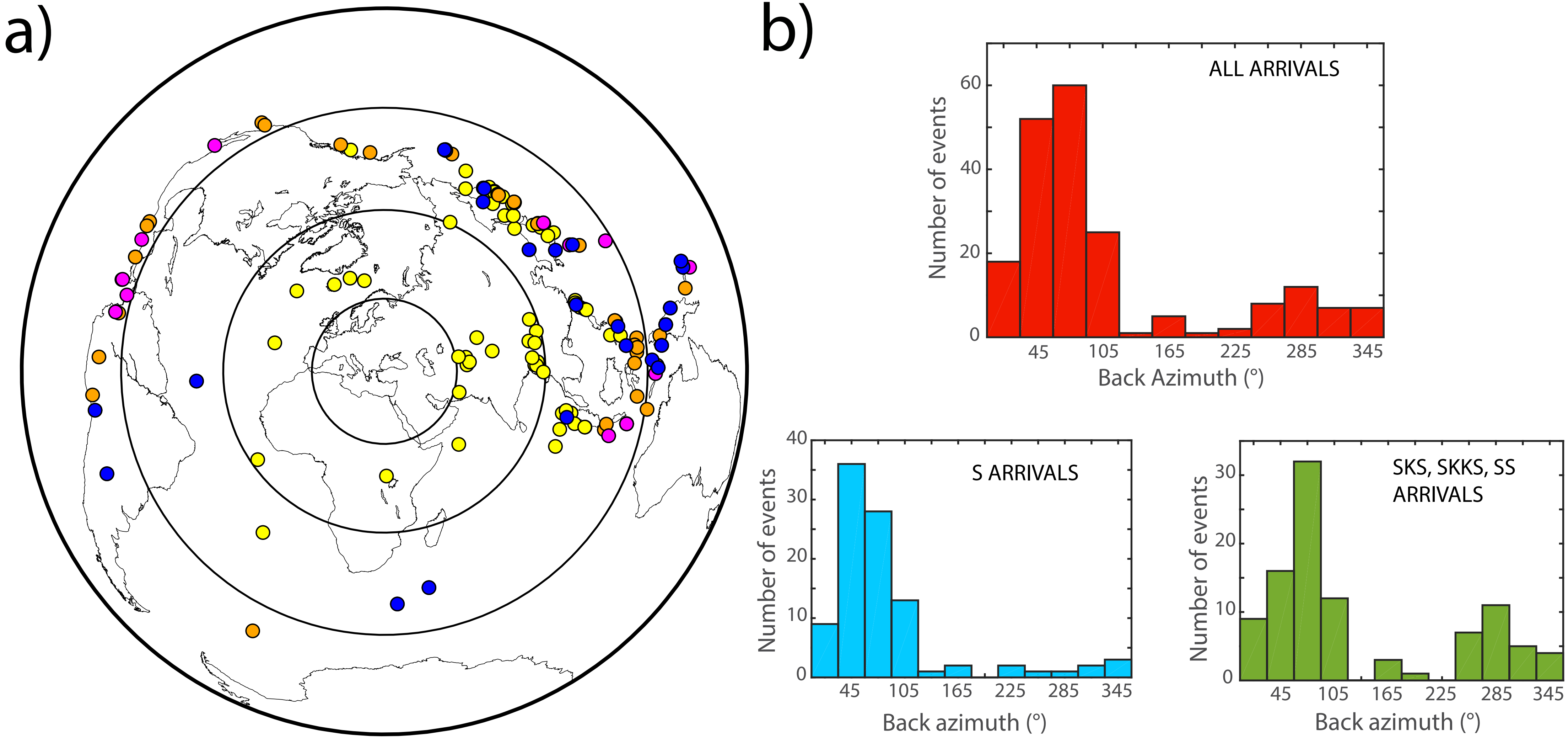
a)
b)
ALL ARRIVALS
Number of events
Back Azimuth (°)
0
20
40
60
45
105
165
225
285
345
S ARRIVALS
Number of events
Back azimuth (°)
0
10
20
30
40
45
105
165
225
285
345
SKS, SKKS, SS
ARRIVALS
Number of events
Back azimuth (°)
0
10
20
30
45
105
165
225
285
345

Fig3.

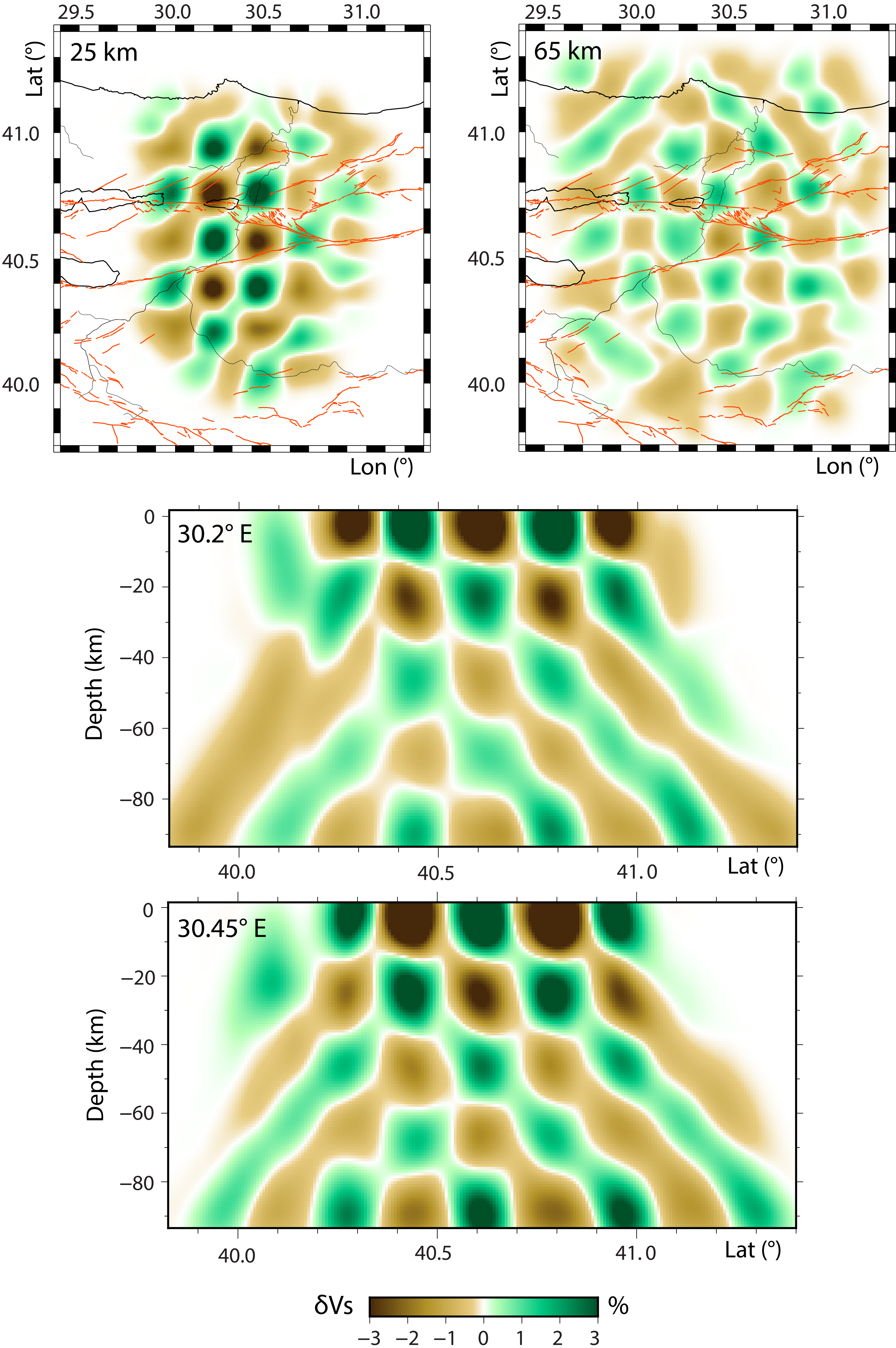

25 km
65 km
Lat (°)
Lon (°)
29.5
30.0
30.5
31.0
41.0
40.5
40.0
30.2° E
30.45° E
Depth (km)
Lat (°)
0
−20
−40
−60
−80
δVs
%
−3
−2
−1
0
1
2
3

Fig4.

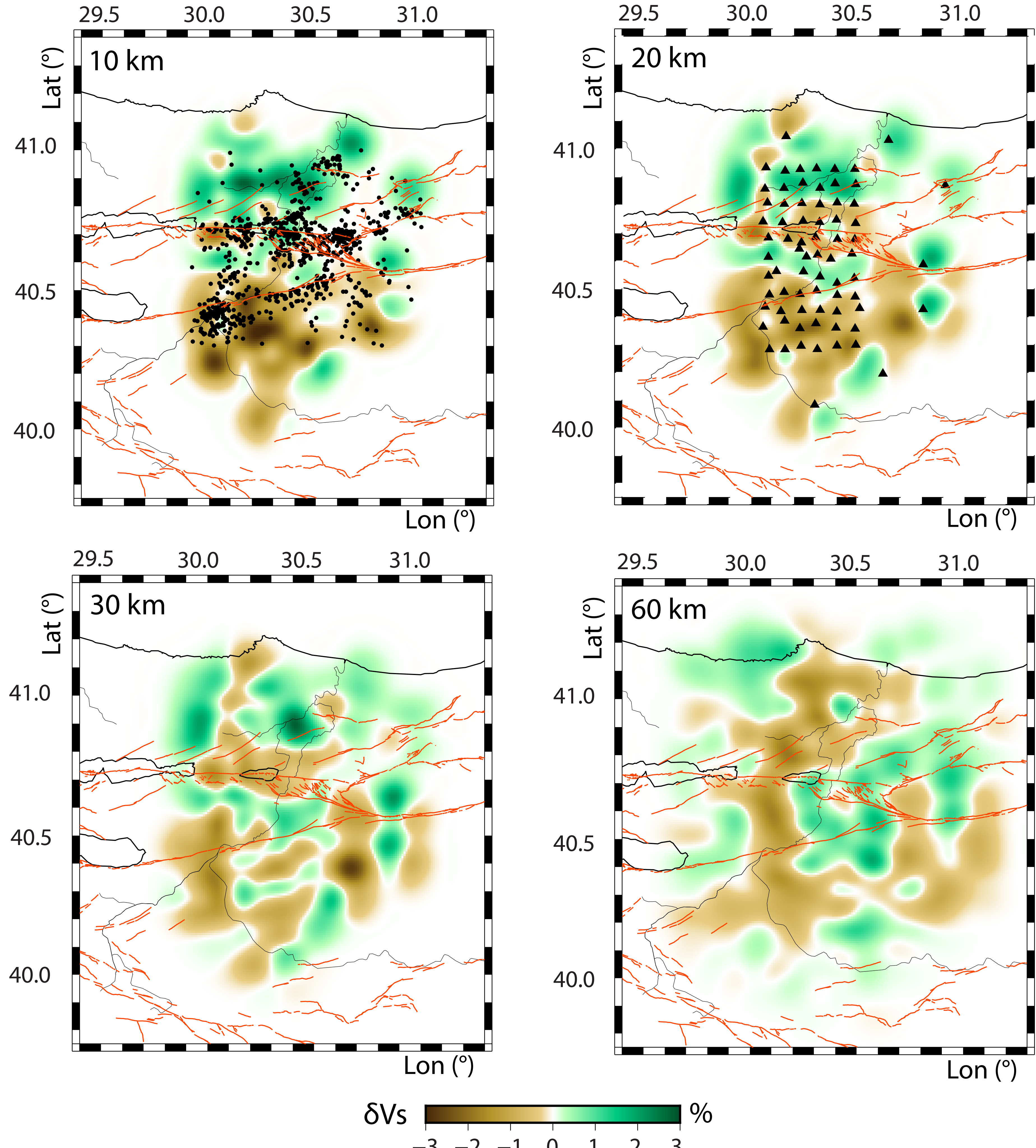

10 km
20 km
30 km
60 km
Lat (°)
Lon (°)
29.5
30.0
30.5
31.0
40.0
40.5
41.0
δVs
%
−3
−2
−1
0
1
2
3

Fig5.

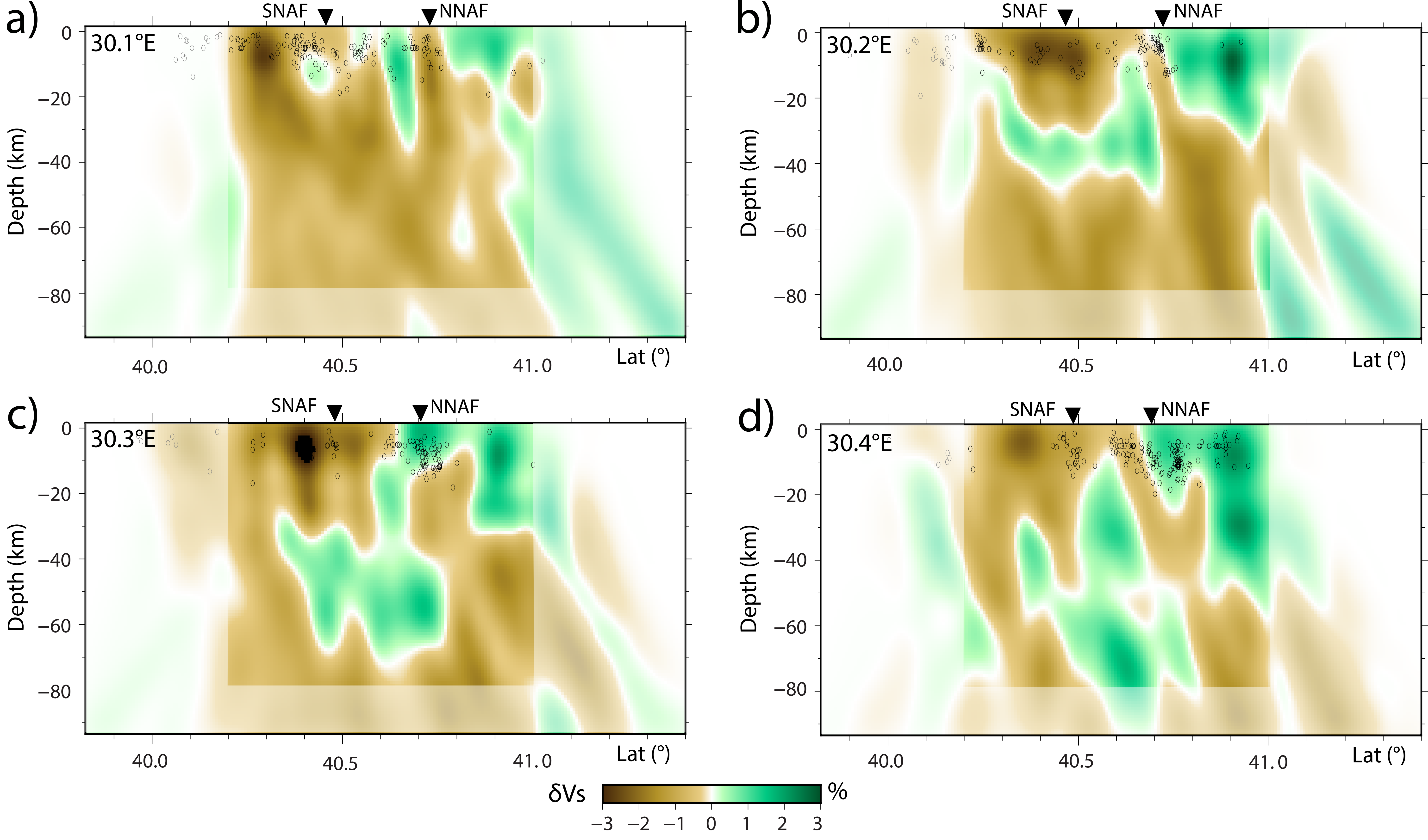

a)
SNAF
NNAF
30.1°E
Depth (km)
Lat (°)
b)
30.2°E
c)
30.3°E
d)
30.4°E
0
−20
−40
−60
−80
40.0
40.5
41.0
δVs
%
−3 −2 −1 0 1 2 3

Fig6.

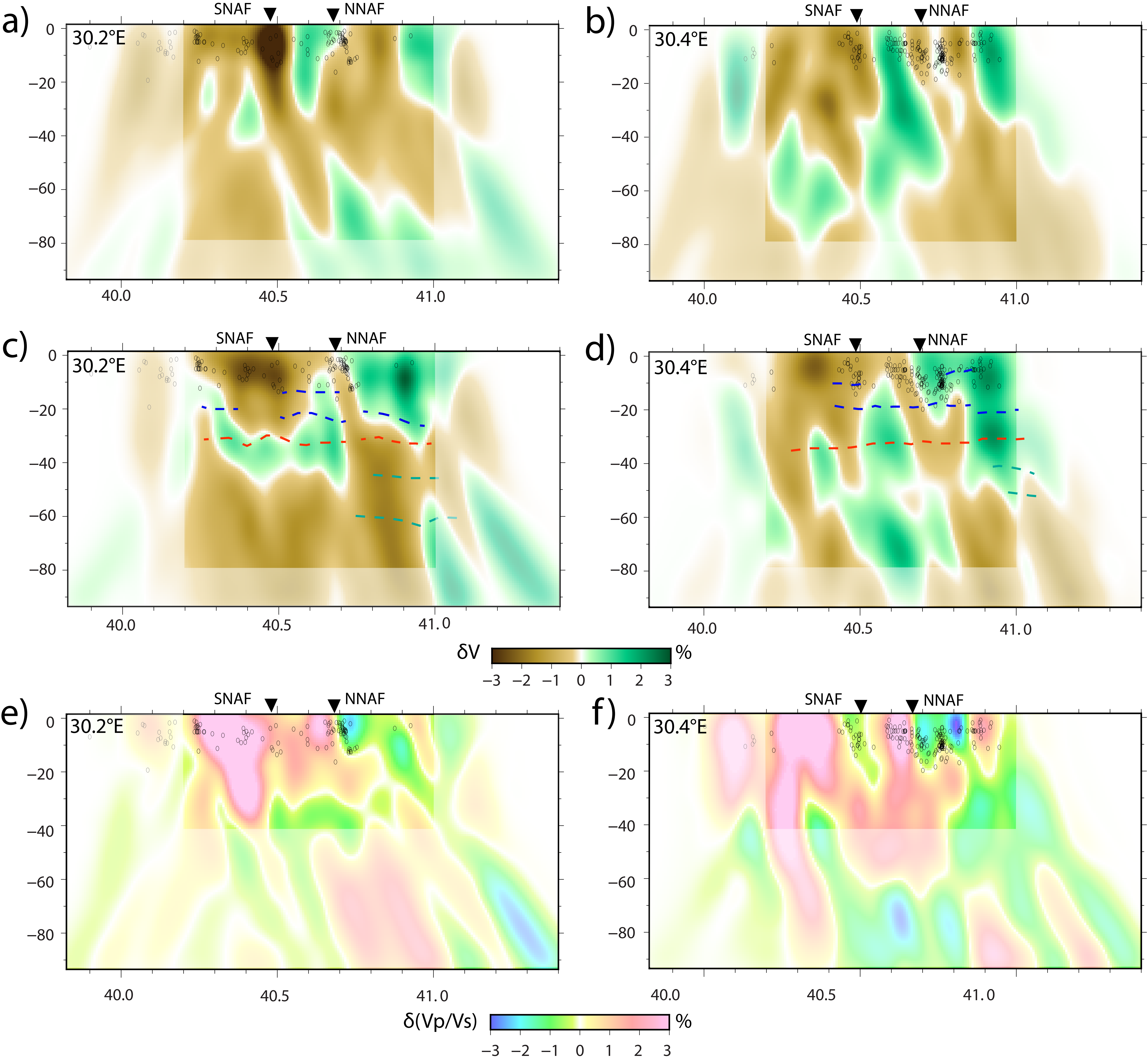

a)
b)
c)
d)
e)
f)
SNAF
NNAF
30.2°E
30.4°E
0
−20
−40
−60
−80
40.0
40.5
41.0
δV
%
−3 −2 −1 0 1 2 3
δ(Vp/Vs)
%
−3 −2 −1 0 1 2 3

Fig7.

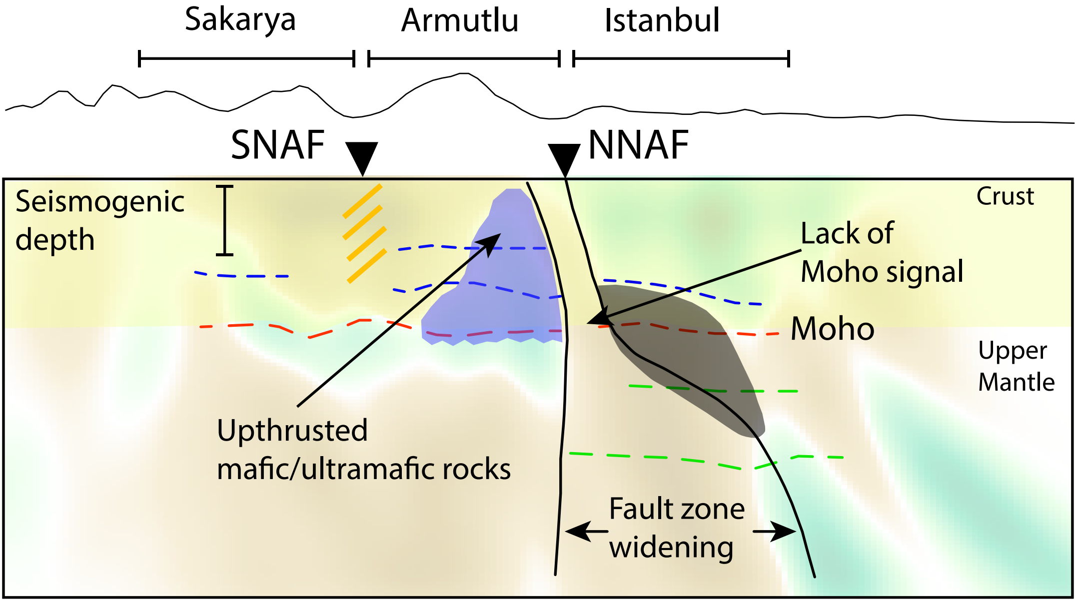
Sakarya
Armutlu
Istanbul
SNAF
NNAF
Seismogenic depth
Crust
Lack of Moho signal
Moho
Upper Mantle
Upthrusted mafic/ultramafic rocks
Fault zone widening